

Discretized Aperture Integration, Surface Integration Analysis of Airborne Radomes

Jared Williams Jordan¹ and Benjamin L. Cannon²

¹Raytheon Missile Systems
Tucson, AZ 85756, USA
jaredwilliamsjordan@gmail.com

²Nuvotronics LLC
Durham, NC 27703, USA
bcannon@nuvotronics.com

Abstract — Full-wave electromagnetic methods are becoming increasingly more viable for the design and analysis of airborne radomes; however, there still exist many applications that require the speed associated with high frequency approximation methods. Presented here are accuracy improvements to the aperture integration surface integration (AiSi) method by incorporating both aperture and radome discretization into smaller groups in advance of the propagation routines, herein referred to as discretized radome discretized aperture integration surface integration (DrDaiSi). Dyadic Green's functions are utilized to determine exact field vectors from source current vectors. The capabilities of DrDaiSi are well-tested for typical airborne radomes, and a case study is presented which includes a 2:1 fineness ratio tangent ogive radome with dielectric constant of 7 and a metallic tip. The benefits of the DrDaiSi algorithm over a non-discretized AiSi method for predicting radome loss, boresight error, and radiation pattern degradation are demonstrated. Results are compared to a full-wave solution of the antenna and radome problem that was solved in CST to represent "truth." Transmission loss agreement is achieved to within 0.4 dB or better, and boresight error agreement is achieved to within 0.2 deg. or better in both elevation and azimuth scan planes for a severely detuned radome.

Index Terms — Airborne radomes, aperture antennas, aperture integration surface integration (AiSi), boresight error (BSE), dyadic Green's functions, monopulse radar.

I. INTRODUCTION

Modern computing resources are capable of performing full-wave electromagnetic simulations of electrically large antenna and radome problems with ever increasing speed and accuracy. As computing technology and commercially-available solvers continue to improve their capabilities, a full-wave approach at

airborne radome design and analysis will continue to become progressively more viable, providing improved accuracy over conventional high-frequency approximation solvers. However, at present-day there still exist many applications where full-wave solvers cannot be used due to prohibitively long run times, or the lack of available computing resources for an accurate solution. Global optimization schemes (*e.g.*, particle swarm, genetic algorithm, etc.) that are often used for antenna and radome design can require hundreds to thousands of iterations depending upon the number of design variables involved. Additionally, simulating radome performance over an entire field-of-regard for various environmental conditions can require a multitude of simulations. Furthermore, multi-layered radome wall configurations often require significant mesh densities to resolve thin layers or fine features along the radome wall, which can result in large RAM usage and excessive computational runtime. For all of the aforementioned reasons, there still exist many benefits of continuing the development of approximation solvers and not to model the entire problem space with full-wave methods.

Over the years, several advances have been made to increase the fidelity of codes utilizing high-frequency approximation methods, and the topic continues to be of interest today. Physical optics (PO) methods and aperture integration surface integration (AiSi) methods [2]-[8] were developed to treat monolithic and layered radomes as scattering objects. In both the PO and AiSi approximations, equivalent electric and magnetic "currents" induced on the radome surfaces are integrated to determine radome effects. For each of these methods, though, the specific propagation functions that are used and the formulation of the scattering currents are what set apart each of the various algorithms that have been developed over the last half-century.

Meng et al. [4] indicate that Paris was the first to integrate the fields incident upon the inner surface of a

radome from an antenna, propagate the energy to the radome outer surface with transmission coefficients, and determine the resulting far-field characteristics by integrating these transmitted fields [9]. Paris spends much of the paper presenting the aperture-integration, surface-integration (AiSi) algorithm formulation, discussing how much of the radome must be included in the final integration to the far-field and how finely sample points should be spaced in the analysis. The author compares far-field pattern measurements to predictions for a horn antenna looking through the nose of a large, asymmetric, well-tuned A-sandwich radome.

Wu and Ruddick replace the aperture integration engine with a plane wave spectrum (PWS) representation of the antenna to determine the fields on the inner radome surface, referring to their algorithm as PWS-SI [10]. The motivation for moving from AI to PWS was to avoid “excessive computation time required for the large number of antenna near-field calculations.” Additionally, the authors state that the individual plane waves in the PWS can be propagated through the radome by applying individual transmission coefficients and then summing the resulting fields on the outer radome surface. Furthermore, the benefit of using a true near-field engine inside the radome, as opposed to ray-tracing, is discussed. Predicted versus measured boresight error results are provided in one principle plane for two well-tuned radomes with corresponding fineness ratios of 1:1 and 2:1.

Shifflett demonstrates the capabilities of a radome analysis code, CADDRAD [11], which can utilize either ray-tracing to model the antenna or an aperture representation much like Paris [9]. The aperture integration version is capable of including a single internal radome bounce, and applies normal incidence transmission coefficients to the one-bounce energy that propagates through the radome. Transmission from the aperture through the radome can be performed at an individual current element-by-element level—which is similar to what will be shown herein—or at the full aperture level. Finally, radome surface currents are integrated to determine far-field radiation patterns. Comparisons between measured and predicted beam peak loss for three beam positions are provided. Additionally, agreement between measured boresight error (BSE) with simulated predictions is presented for a single scan plane.

The current paper outlines and demonstrates an aperture integration surface integration algorithm which utilizes dyadic Green’s functions as the current-to-field propagator. Furthermore, both the aperture and radome are discretized into groups before the resulting propagated fields are transmitted through the radome. The authors refer to the algorithm as discretized radome, discretized aperture integration, surface integration (DrDaiSi). Additionally, DrDaiSi has the ability to model as many internal radome reflections as necessary for

electromagnetic predictions of interest to reach satisfactory convergence. Far-field radiation patterns are predicted at three radome scan directions of interest and antenna boresight radome transmission and boresight errors in both the azimuth and elevation plane are compared to full-wave simulations. The prediction capabilities of DrDaiSi are well-tested for typical airborne radomes, as the presented radome case study possesses a large metallic tip, is significantly detuned, possesses a fineness ratio of 2:1, and the edge of the enclosed antenna are located within fractions of a wavelength to the radome wall.

II. FORMULATION OF DRDAISI

As was stated previously, DrDaiSi is an aperture integration surface integration (AiSi) code which includes discretization of the aperture surface—as well as the inner radome surface—into groups prior to the propagation, transmission, and integration algorithm procedures. This method involves the linear superposition of transmitted fields through the radome from these discretized groups. This simple modification will be shown to result in significant improvements over non-discretized AiSi for modeling the effects of a radome on an enclosed antenna when the antenna is in close proximity to the radome. Additionally, well-chosen aperture and radome group sizes can speed up computation time without significantly impacting accuracy.

DrDaiSi will first be briefly outlined, then details of the algorithm will be provided:

- 1) *The inner surface of the radome is meshed using triangular facets. The dimensions of each facet are chosen such that they are small in comparison to the operating frequency wavelength and will ultimately produce converged results for the model predictions of interest; e.g., far-field radiation patterns, boresight errors, boresight radome loss.*
- 2) *Electric and magnetic currents that comprise the aperture are discretized into aperture groups in preparation for propagation to the radome inner surface.*
- 3) *For each individual aperture group, the induced electric and magnetic fields at the inner surface of the radome are calculated.*
- 4) *For each individual aperture group, the resultant reflected and transmitted fields on the radome surface are calculated using planar transmission and reflection coefficients.*
- 5) *The total transmitted fields from all aperture groups are translated to the outer surface of the radome, converted to equivalent currents and propagated to the far-field.*
- 6) *The total reflected fields are converted to equivalent currents. These equivalent currents are discretized into radome groups, each of which is individually radiated to the entire radome inner surface.*

- 7) For each radome group, the resultant transmitted and reflected fields on the radome surface are calculated using planar transmission and reflection coefficients.
- 8) The total transmitted fields from all radome groups are moved to the outer surface of the radome, converted to equivalent currents and propagated to the far-field.
- 9) Steps 6-8 represent the propagation bounce energy within the radome and are repeated for as many bounces as are required to achieve satisfactory convergence for the model prediction parameters of interest.

The equations for the full dyadic Green's functions (DGFs) in a homogenous and isotropic region are derived in Diaz and Milligan [12] and are summarized below. The DGFs are convenient as current-to-field propagators. The DGFs transform current sources, with arbitrary coordinates and vector components in a Cartesian coordinate system into corresponding field vectors defined at any observation point in a homogenous and isotropic medium. This enables one to keep track of the polarization of the radiated fields with respect to the source currents. The first type of DGF is used in the calculation of an electric field \mathbf{E} due to an electric current \mathbf{J} , denoted as $\underline{\underline{G_{EJ}}}$ and a magnetic field \mathbf{H} due to a magnetic current \mathbf{M} , denoted as $\underline{\underline{G_{HM}}}$, as shown in (1). The difference between the two being the replacement of ε with μ , in $\underline{\underline{G_{HM}}}$ to produce $\underline{\underline{G_{EJ}}}$; as the duality theorem dictates [13]:

$$\underline{\underline{G_{EJ}}}(\mathbf{R}) = \frac{\mu}{\varepsilon} \underline{\underline{G_{HM}}}(\mathbf{R}) = j\omega\mu \frac{e^{-jkR}}{4\pi R} \underline{\underline{X}}, \quad (1)$$

where, $\underline{\underline{X}}$ is defined as:

$$\underline{\underline{X}} = \left[\left(\mathbf{1} - \hat{\mathbf{R}}\hat{\mathbf{R}}^T \right) \left(1 - \frac{1}{k^2 R^2} - j \frac{1}{kR} \right) + \hat{\mathbf{R}}\hat{\mathbf{R}}^T \left(\frac{2}{k^2 R^2} + j \frac{2}{kR} \right) \right]. \quad (2)$$

The second type of DGF is used for the calculation of a magnetic field due to an electric current, denoted as $\underline{\underline{G_{HJ}}}$ and an electric field due to a magnetic current, denoted as $\underline{\underline{G_{EM}}}$, as is provided in (3). The difference between the two being the replacement of +1 factor with a -1 factor, in $\underline{\underline{G_{HJ}}}$ to produce $\underline{\underline{G_{EM}}}$; as also dictated by the duality theorem:

$$\underline{\underline{G_{EM}}}(\mathbf{R}) = -\underline{\underline{G_{HJ}}}(\mathbf{R}) = -\frac{e^{-jkR}}{4\pi R} \left(\frac{1}{R} + jk \right) \hat{\mathbf{R}} \times \underline{\underline{1}}, \quad (3)$$

where, $\hat{\mathbf{R}} \times \underline{\underline{1}} = (\hat{\mathbf{R}} \times \hat{\mathbf{x}})\hat{\mathbf{x}}^T + (\hat{\mathbf{R}} \times \hat{\mathbf{y}})\hat{\mathbf{y}}^T + (\hat{\mathbf{R}} \times \hat{\mathbf{z}})\hat{\mathbf{z}}^T$ and $\hat{\mathbf{x}}, \hat{\mathbf{y}}$, and $\hat{\mathbf{z}}$ are Cartesian unit column vectors. More details on dyadic Green's functions can be found in [12]-[15].

The above DGFs utilize the transport distance column vector, \mathbf{R} , and its unit normal, $\hat{\mathbf{R}}$, (4), where primed coordinates refer to source current locations and unprimed coordinates refer to field observation positions:

$$\hat{\mathbf{R}} = \frac{\mathbf{R}}{R} = \frac{\mathbf{r} - \mathbf{r}'}{|\mathbf{r} - \mathbf{r}'|} = \frac{1}{\sqrt{(x-x')^2 + (y-y')^2 + (z-z')^2}} \begin{bmatrix} x-x' \\ y-y' \\ z-z' \end{bmatrix}. \quad (4)$$

The resulting four DGFs, $(\underline{\underline{G_{EJ}}}, \underline{\underline{G_{HM}}}, \underline{\underline{G_{EM}}}, \underline{\underline{G_{HJ}}})$, then

provide the electric and magnetic fields at an observation location \mathbf{r} due to a source described by an electric current element and a magnetic current element. The resulting fields from the individual currents are summed, via superposition [13], to produce the overall source current distribution's electric and magnetic field responses, (5) and (6) respectively:

$$\mathbf{E}(r, \mathbf{J}, \mathbf{M}) = -\iint_{S'} \underline{\underline{G_{EJ}}}(\mathbf{R}) \cdot \mathbf{J}(\mathbf{r}') dS' - \iint_{S'} \underline{\underline{G_{EM}}}(\mathbf{R}) \cdot \mathbf{M}(\mathbf{r}') dS', \quad (5)$$

$$\mathbf{H}(r, \mathbf{J}, \mathbf{M}) = -\iint_{S'} \underline{\underline{G_{HJ}}}(\mathbf{R}) \cdot \mathbf{J}(\mathbf{r}') dS' - \iint_{S'} \underline{\underline{G_{HM}}}(\mathbf{R}) \cdot \mathbf{M}(\mathbf{r}') dS'. \quad (6)$$

DrDaiSi differs from non-discretized AiSi in how it propagates energy from the aperture through the radome. Rather than radiating the entire aperture to the radome inner surface and applying transmission/reflection coefficients to these total fields, the aperture is instead discretized into smaller, user-specified aperture groups whose energy is propagated through the radome individually. Without aperture discretization, a radome observation point often exists in the near-field of the enclosed aperture. Consequently, any near-field component existing along the primary direction of propagation is lost during the conversion to perpendicular and parallel components before the application of the transmission/reflection coefficients. By discretizing the aperture into smaller groups, the radiative far-field distance for the aperture groups become much shorter, and the radome thus exists in the far-field of the smaller aperture groups. Under this condition, negligible energy is lost during the conversion to perpendicular and parallel components, yielding more accurate results.

To appreciate the discretized aperture concept, the authors find it beneficial to draw comparisons to the plane wave spectrum (PWS) method for calculating electromagnetic fields. PWS is a transformation of the aperture fields into a set of propagating and non-propagating plane wave modes which emanate from the aperture plane in all directions. In practice, though, this expansion is typically truncated to a finite number of modes. At an observation point on the radome surface, the superposition of these plane waves can then recreate the near and far fields above the aperture plane. The radiation from a discretized aperture via DGFs is the

summation of electric and magnetic dipoles defined within individual aperture groups, whose phase centers correspond to the physical locations of the aperture groups. In this case, a point on the radome's inner surface "observes" a set of spherical waves radiating from each of the aperture group's phase center, which is a similar observation to what is witnessed during the PWS method when aperture groups are sufficiently small. Said another way, a point on the radome surface observes a finite set of spherical waves, instead of a finite set of plane waves, propagating from several different directions.

To ensure the radome is sufficiently in the far-field of each of the aperture groups, the following condition should be met [16], where D is the largest extent of the aperture group:

$$\text{FraunhoferRegion (Far-Field): } R > \frac{2D^2}{\lambda}. \quad (7)$$

It should be noted that by meeting the above far-field condition (7), the user may decide to remove the $1/R^2$ and $1/R^3$ terms in the DGFs to reduce the calculation time of the algorithm. The authors decided against this since the improvement in calculation time was not appreciable enough to warrant this additional approximation to the method. Furthermore, by discretizing the aperture into well-chosen aperture group sizes, minimal energy is lost in the direction of propagation, and excessive calculations of transmission/reflection coefficients are avoided, since it is not necessary to perform this operation for every individual current element.

Before transmission and reflection coefficients can be determined for energy incident upon an inner radome surface triangular facet, the unit Poynting vector is calculated from [9]:

$$\hat{\mathbf{s}} = \frac{\text{Re}(\mathbf{E}_i \times \mathbf{H}_i^*)}{\left| \text{Re}(\mathbf{E}_i \times \mathbf{H}_i^*) \right|}. \quad (8)$$

The energy propagation direction is then used to determine the angle of incidence with respect to the facet's normal, which points into the radome.

The incident field energy is modified by transmission and reflection coefficients to determine the amount of energy that will leave the radome, to propagate to the far-field, and how much energy will be reflected and re-propagated inside the radome as bounce energy. These coefficients describe the behavior of a plane wave incident upon a flat wall of infinite extent. It is this approximation that removes the necessity of meshing the multiple layers that may compose the radome wall. A significant advantage of modeling an antenna/radome system with an aperture integration, surface integration method is the freedom in defining the transmission and reflection coefficients; they can be analytic expressions, numerically determined, experimentally measured or a combination of all. The presented antenna/radome problem made use of Fresnel coefficients [15].

Calculation of the transmitted fields through the radome is as follows. The incident fields are decomposed into perpendicular and parallel components, the corresponding orthogonal transmission coefficients are applied, and the modified field components are recombined. This process is summarized in (9) and (10), where the perpendicular and parallel transmission coefficients, T_{\perp} and $T_{//}$, are defined with respect to the electric field vector. Magnetic fields are orthogonal to electric fields and as such the parallel transmission coefficient is used to modify the perpendicular component of the magnetic field and vice versa:

$$\mathbf{E}_T = (\mathbf{E}_i \cdot \hat{\mathbf{u}}_{\perp}) T_{\perp} \hat{\mathbf{u}}_{\perp} + (\mathbf{E}_i \cdot \hat{\mathbf{u}}_{//}) T_{//} \hat{\mathbf{u}}_{//}, \quad (9)$$

$$\mathbf{H}_T = (\mathbf{H}_i \cdot \hat{\mathbf{u}}_{\perp}) T_{//} \hat{\mathbf{u}}_{\perp} + (\mathbf{H}_i \cdot \hat{\mathbf{u}}_{//}) T_{\perp} \hat{\mathbf{u}}_{//}. \quad (10)$$

Similarly, the reflected fields (11) and (12) are calculated [6]:

$$\mathbf{E}_R = (\mathbf{E}_i \cdot \hat{\mathbf{u}}_{\perp}) R_{\perp} \hat{\mathbf{u}}_{\perp} + (\mathbf{E}_i \cdot \hat{\mathbf{u}}_{//}) R_{//} \hat{\mathbf{u}}_{//}, \quad (11)$$

$$\mathbf{H}_R = (\mathbf{H}_i \cdot \hat{\mathbf{u}}_{\perp}) R_{//} \hat{\mathbf{u}}_{\perp} + (\mathbf{H}_i \cdot \hat{\mathbf{u}}_{//}) R_{\perp} \hat{\mathbf{u}}_{//}. \quad (12)$$

As a first order approximation, the radome tip is modeled as a perfect electric conductor (PEC) and is treated as a simple blockage. All energy incident on a radome facet defined as PEC is reflected back into the radome. To account for the reflection from a perfect electric conductor using Fresnel coefficients, the following approximation is used [17]:

$$\text{PEC Approx: } \epsilon_r = 1 - j100,000; \quad \mu_r = 1 - j0. \quad (13)$$

Every inner radome surface facet has a corresponding outer radome surface facet. Each triangular facet is defined by three nodes. The facets surrounding each node are determined and the following is performed to determine the location of the outer facet node locations:

$$\text{Node}_{Outer} = \text{Node}_{Inner} + \frac{\sum_{n=1}^N FT_n \mathbf{FN}_n}{N}, \quad (14)$$

where N is the number of facets surrounding the node, FT is the facet thickness and \mathbf{FN} is the facet unit normal.

Fields that are transported to the outer radome surface, from direct aperture illumination and consecutive bounce energy, are converted to current sources:

$$\mathbf{J}_s = \hat{\mathbf{n}} \times \mathbf{H}, \quad \mathbf{M}_s = -\hat{\mathbf{n}} \times \mathbf{E}, \quad (15)$$

where $\hat{\mathbf{n}}$ is the outer surface normal. Electric and magnetic fields that are not transmitted through the radome from direct aperture illumination or consecutive radome bounce energy are also converted to tangential magnetic and electric currents (15), and serve as the consecutive bounce source currents. The radome was discretized into 4 longitudinal quadrants, defined by the intersection of the XZ and YZ planes when the radome is gimballed to 0 deg. in azimuth and elevation. The radome quadrants are herein referred to as radome groups. Discretizing the radome into more groups did not produce better results. The authors believe that since the

radome is sourcing itself during bounce-energy propagation—often at grazing incidence—the determination of radome group size is not as well-defined as aperture group size. This is a topic of ongoing investigation.

The resulting bounce source currents are used to rattle energy within the radome, where transmitted fields at the outer radome surface from each radome group are summed via superposition in preparation for computation of far-field quantities of interest. After all, bounce energy has left the radome and outer surface currents have converged, the resultant outer radome surface currents are an approximation to the equivalence principle [13]. The antenna and radome are removed and a sheet of tangential electric and magnetic currents radiates in their place. It is only an approximation to equivalence principle since the sheet of current does not fully enclose the antenna and radome system, and any fields propagated to the aperture plane are neglected. It is believed that inclusion of these currents, in the computation of boresight radome loss and errors, possesses a relatively low impact for practical airborne radomes.

Converged tangential currents on the outer radome surface are then propagated to the far-field to calculate radiation patterns, boresight radome loss (16) and boresight errors (17), (18), where S_{EL} and S_{AZ} represent the monopulse slope values of the aperture in the elevation and azimuth planes, respectively [18]. The sum and delta patterns are formed from radiating the quadrants individually and applying superposition to the far-fields. Symmetry was utilized in the principle plane scans, and as a result only two of the four quadrants were needed per radome look direction in both the azimuth and elevation planes:

$$\text{RadomeLoss} = 20 \log_{10} \left(\frac{E_{far_SUM}(\text{Radome})}{E_{far_SUM}(\text{AirRadome})} \right), \quad (16)$$

$$BSE_{EL} = \frac{1}{S_{EL}} \text{imag} \left(\frac{E_{far_NEL}}{E_{far_SUM}} \right), \quad (17)$$

$$BSE_{AZ} = \frac{1}{S_{AZ}} \text{imag} \left(\frac{E_{far_AAZ}}{E_{far_SUM}} \right). \quad (18)$$

III. RADOME/ANTENNA PROBLEM UNDER INVESTIGATION

The radome and antenna system under evaluation was also used as a case study in the authors' previous paper [19] and will be shown again here in Fig. 1 and its dimensions will be restated for completeness of this paper. The antenna diameter is 10 in. and consists of 4 quadrants, each containing 17 half-wavelength resonant slots [20] designed for operation at 7 GHz. Each slot is individually fed by a WR-137 waveguide located behind the ground plane. The radome is a tangent ogive with an approximate fineness ratio of 2:1, inside base radius of 11 in., and an inner length of 22 in. The radome gimbal

center is positioned 4 in. into the radome from its base. The plane that the slots reside in is located 1 in. from the gimbal center. The edge of the antenna is less than 0.25 in. (15% of a freespace wavelength at 7 GHz) from the inside of the radome. The top 1 in. of the radome is a metal tip, modeled as a perfect electric conductor (PEC). The radome shell is 0.3 in. thick and is constructed from a lossless dielectric with a relative permittivity of 7. The thickness of the radome wall was intentionally chosen to provide a detuned response at the operating frequency of 7 GHz to demonstrate the presented modeling methodology in a circumstance where significant bounce energy exists.

The normal of the antenna faceplate is directed along the positive z-axis and the radiating slots are y-polarized. The elevation plane is defined as the YZ plane, and the azimuth plane is defined as the XZ plane. The radome is gimballed about the gimbal center, while the antenna is fixed and results will be presented as such.

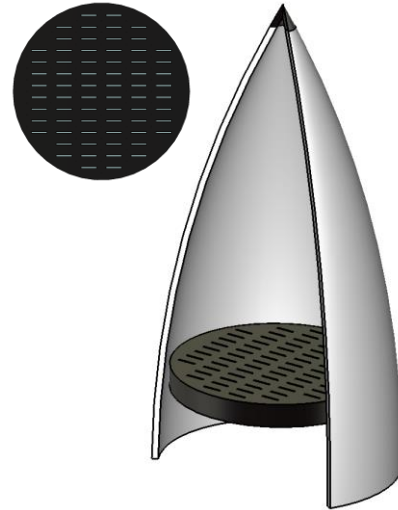


Fig. 1. Radome and antenna geometry under evaluation. The antenna is an array of 68 half-wavelength resonant radiating slots and is in close proximity to the radome.

IV. RADOME MODELING RESULTS AND DISCUSSION

In a previous publication by the authors [19], the same antenna and radome problem is analyzed, where the antenna and radome simulated together in a full-wave solver is presented as “truth” and is used as the baseline for comparison to quantify the accuracy of the proposed modeling method. Similarly, this paper will use the same baseline results to quantify the performance of DrDaiSi. However, the results corresponding to the equivalent aperture, used in conjunction with CST’s full-wave solver, will not be revisited here since it is not the focus of this paper. Instead, the reader is encouraged to compare the results of the two antenna/radome methods and determine which of the two better serves their needs.

Furthermore, both modeling methods utilize the same equivalent aperture representation of the radiating slot antenna quads and the reader is referred to the author's previous publication to understand how they are formed [19].

The normalized magnitude of the electric field transmitted to the outer radome surface from direct quadrant 1 aperture illumination and the three consecutive bounces is illustrated in Fig. 2. Transmitted electric fields from direct aperture illumination are presented in Figs. 2 (a) and (b), where the radome is oriented in the XY and the XZ planes, respectively. As it can be seen, most of the energy is focused on the part of the radome existing in the first quadrant, indicating that the aperture is well-collimated. The magnitude of the transmitted field for the first bounce, Fig. 2 (c), is a clear indicator that the radome is detuned and bounce energy should be considered in the analysis. The magnitudes of the transmitted fields for the second radome bounce are significantly lower, Fig. 2 (d), but are still present. It is not until the third radome bounce, Fig. 2 (e), that the transmitted fields are significantly lower (less than the 30 dB colormap range) than the transmitted fields from direct aperture illumination. For this case study, including bounce energy past three iterations had a negligible impact on far-field radiation patterns, boresight radome loss and boresight error.

The transmitted fields on the outer radome surface in Fig. 2 incorporated discretization of the aperture and the radome. In an effort to demonstrate the impact of aperture and radome discretization on far-field results, DrDaiSi is also compared to the scenario where the aperture radiates as a whole to the radome and the entire inner radome surface serves as a source to itself as one group for consecutive bounce iterations; herein this scenario will be referred to as AiSi.

Far-field patterns for the antenna looking out the nose of the radome are presented in Figs. 3 (a) and (b), where normalized gain values are calculated in the elevation and azimuth planes. Normalization is with respect to the peak antenna/aperture only results. Full-wave results are obtained using CST's finite integration technique solver and are labeled accordingly. In reference to the elevation plane, AiSi incorrectly predicts the magnitude of the main beam, and is quantified in Fig. 6. In addition to over predicting the boresight antenna/aperture gain by almost 1.5 dB, the structure of the main beam is not captured. In contrast, the DrDaiSi results are much better; the boresight antenna/aperture gain is approximately 0.4 dB too large and the main beam structure is better captured. Furthermore, AiSi predicted first null and first sidelobe are poorly predicted and their locations are off by 3 deg. in the elevation plane, whereas DrDaiSi captures this behavior well within 1 deg. With respect to both the azimuth and elevation far-field patterns, the peak sidelobe levels are predicted by AiSi within 5-6 dB and within

2-3 dB by DrDaiSi. However, both methods begin to deviate from the full-wave CST results past 60 deg., where alignment of sidelobe peaks and nulls falls apart and magnitudes of sidelobe peaks can be greater than 5 dB from "truth." This is largely in part due to the fact that the antenna is represented by an equivalent aperture.

The elevation plane farfield patterns, for radome gimbal direction of 0 deg. azimuth and 20 deg. elevation is presented in Fig. 4. This radome look direction is of particular interest since it demonstrates significant deflection of the main beam, as is shown in Fig. 7 (a) to be approximately 1 deg. DrDaiSi accurately predicts the far-field response but starts to deviate from CST past -60 deg. AiSi does not perform as well; the transmission prediction is too high, the first sidelobe levels are approximately 2 dB too large, and the rippled sidelobe behavior that occurs near 60 deg. is not well-captured. This ripple in the sidelobes is a product of the constructive and destructive interference of scattered energy transmitted through the radome, and is non-existent for antenna-only radiation.

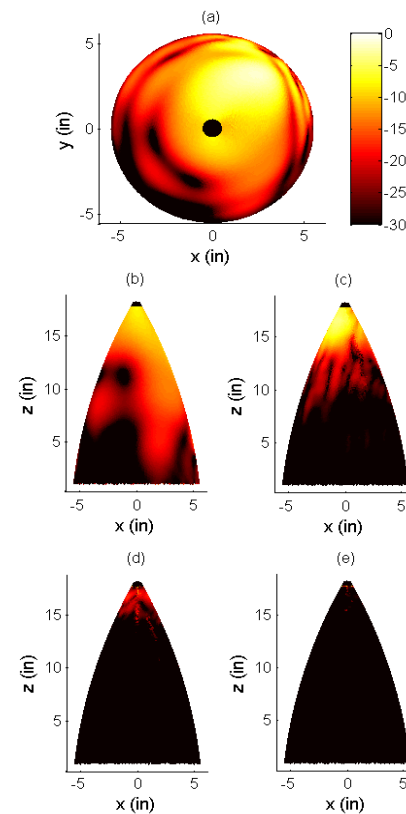


Fig. 2. Normalized magnitude of the transmitted electric fields from direct Quadrant 1 aperture illumination and bounce energy when the radome is gimbaled 0 degrees in azimuth and 0 degrees in elevation. Transmitted fields are a result of: (a) direct aperture illumination, (b) direct aperture illumination (c) first radome bounce, (d) second radome bounce, and (e) third radome bounce.

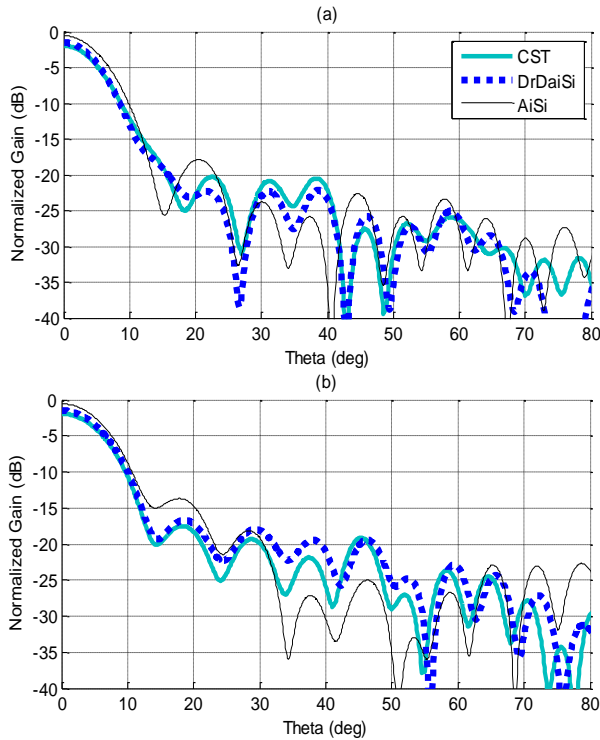


Fig. 3. Effect of radome on antenna/aperture far-field patterns where the radome is gimbaled 0 degrees in azimuth and 0 degrees in elevation. (a) Far-field patterns in EL-plane, and (b) far-field patterns in AZ-plane. Patterns are normalized to peak antenna/aperture far-field value.

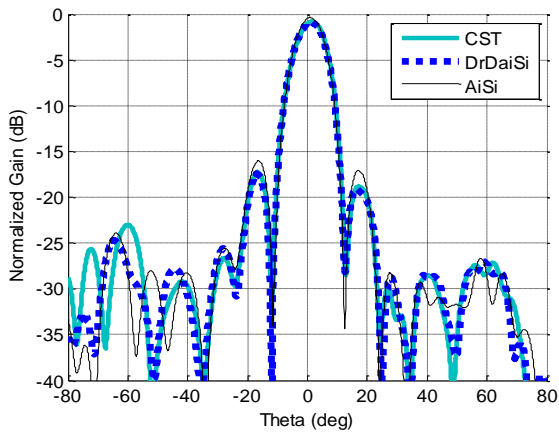


Fig. 4. Effect of radome on antenna/aperture EL-plane far-field patterns where the radome is gimbaled 0 degrees in azimuth and 20 degrees in elevation. Patterns are normalized to peak antenna/aperture far-field value.

The last presented radome look direction of interest, with respect to far-field patterns, is radome gimbal direction of 14 deg. azimuth and 0 deg. in elevation, provided in Fig. 5. Here, an interesting phenomenon referred to as a

“bounce lobe” or “flash lobe” appears centered around 55 deg. Bounce lobes are typically dominant in an H-plane scan where radome transmission is dominated by perpendicular polarized energy. The dominant energy constructing a bounce lobe is the energy from the first bounce reflecting from the radome back wall, transmitting through the front wall. Often this reflection occurs on the back wall close to the radome tip, as is with the case of the current radome under investigation. The nose of the radome is where small radii of curvature exist and where the current modeling method starts to break-down. To increase the accuracy of the proposed method a full-wave solver such as method of moments could be incorporated with the presented modeling method to capture a more representative scattering effect from the radome tip [1]. With that being said, both DrDaiSi and AiSi capture the presence of a flash lobe with the correct number of peaks and valleys with corresponding magnitude values within 3-4 dB from CST. DrDaiSi does outperform AiSi with respect to peak main beam normalized gain by deviating from “truth” by only 0.1 dB as opposed to almost 1 dB, see Fig. 6 (b).

The presented farfield radiation patterns indicate the presence of boresight transmission loss and boresight errors, but it is difficult to quantify their values from the radiation pattern plots with much accuracy; therefore, the data will be presented in a more digestible form. Boresight radome loss and errors are calculated using (16) through (18) for both the elevation and azimuth planes in Fig. 6 and Fig. 7. Boresight radome loss will be presented with the scale of zero attenuation to half-power loss. In the case of this radome, the energy is not lost to a dielectric loss tangent, but rather to re-radiation of energy into different directions, resulting in the distortion of the main-beam and an increase in side lobe levels.

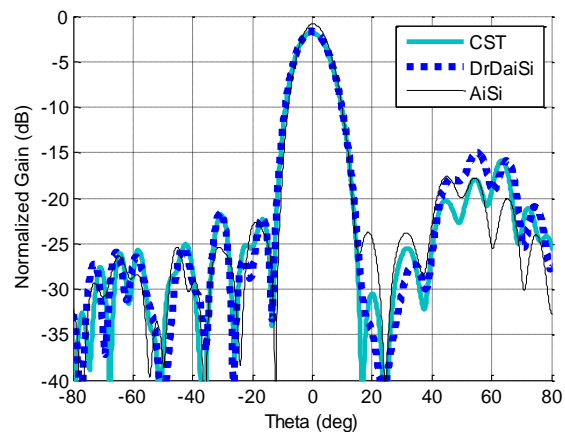


Fig. 5. Effect of radome on antenna/aperture AZ-plane far-field patterns where the radome is gimbaled 14 degrees in azimuth and 0 degrees in elevation. Patterns are normalized to peak antenna/aperture far-field value.

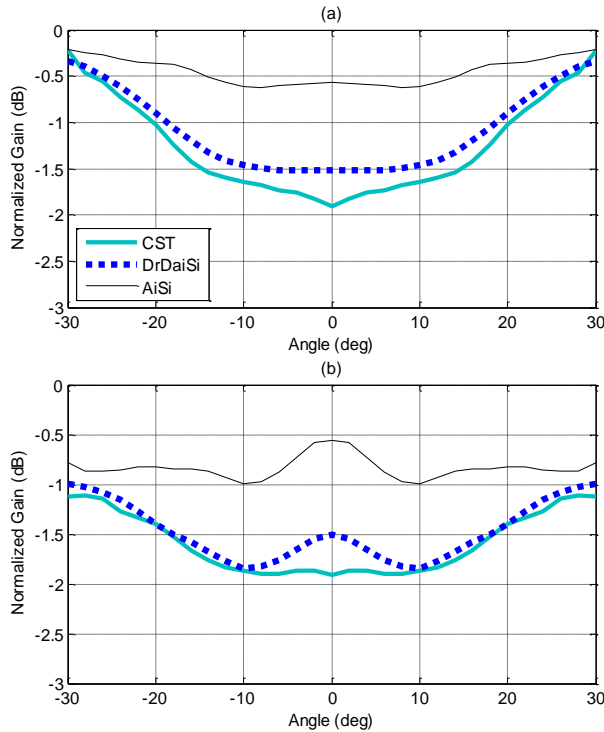


Fig. 6. Effect of radome on antenna/aperture bore-sight transmission as radome is gimbaled in the: (a) elevation and (b) azimuth planes. Transmission values are normalized to antenna/aperture bore-sight transmission.

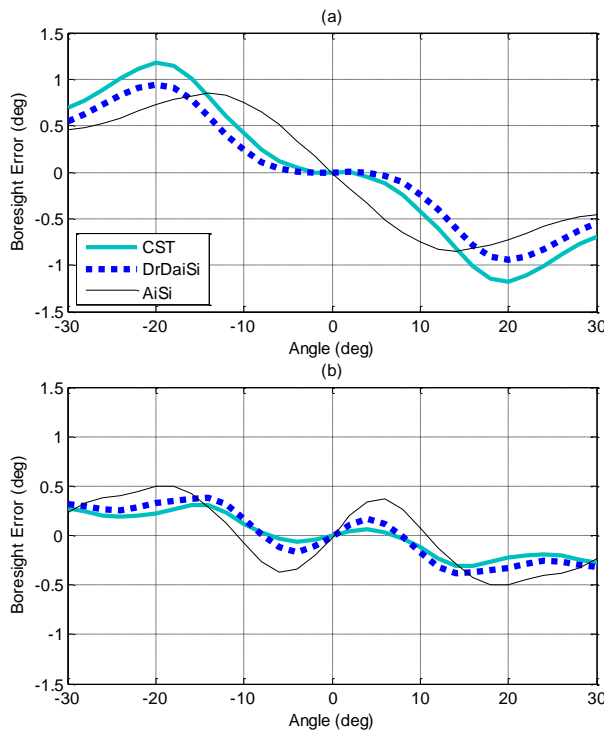


Fig. 7. Antenna/Aperture bore-sight error as radome is gimbaled in the: (a) elevation and (b) azimuth planes.

In reference to Fig. 6, a couple of important observations can be quickly deduced. Firstly and most importantly, the AiSi results deviate from CST significantly more than DrDaiSi. The worst agreement for both modeling methods corresponds to the antenna/aperture looking out the radome nose, where AiSi over predicts the gain by 1.3 dB and the DrDaiSi predicted gain value is almost 1 dB closer to “truth”. The effect of incorporating the discretized aperture and radome into the aperture integration, surface integration algorithm has a significant impact on improving the accuracy of predicted gain values.

Furthermore, the limitations of the proposed method are also illustrated in Fig. 6. By comparing the DrDaiSi and CST results starting from the antenna/aperture looking out the radome nose to looking out the side of the radome, an increase in correlation is witnessed. Additionally, the DrDaiSi results are consistently higher than CST along both cuts, with the peak gain discrepancy corresponding to looking out the radome nose. These results indicate that too much energy is being propagated from the radome outer surface to the far field. The radome nose is where the smallest radi of curvature exist and where inner surface facets grow to correspondingly larger outer surface facets, as dictated by (14). Planar transmission coefficients assume the incident surface is equal in area to the transmission surface. In an attempt to more accurately represent the fields toward the radome tip, the fields could be tapered down as a result of the outer surface growth. The proposed method could possibly benefit from some sort of divergence factor and could be a topic for further investigation.

In reference to Fig. 7, the benefit of the discretized aperture and radome can be clearly seen in the boresight error results. The location of CST’s peak BSE is 20 deg. in the elevation plane and 14 deg. in the azimuth plane, both accurately predicted by DrDaiSi. AiSi incorrectly predicts the maximum BSE locations to be 14 deg. in the elevation plane and 19 deg. in the azimuth plane, which is a 5-6 deg. deviation from “truth”. The boresight error slope is also better captured by DrDaiSi, especially through the radome nose in the elevation plane. However, DrDaiSi’s predicted peak BSE magnitude is off from CST by approximately 0.2 deg. in the elevation plane. Keeping in mind all of the modeling difficulties associated with this specific antenna/radome case study, i.e., high fineness ratio, detuned wall design, large metal tip, antenna/aperture in close proximity to the radome, some prediction inaccuracies associated with utilizing a high frequency approximation technique are expected.

Bore-sight error can be a very sensitive radome characteristic. The presence of a metal tip can affect the boresight error out to large radome gimbal angles even when the tip is outside the main beam of energy propagating from the antenna/aperture. If more accuracy is desired in predicting boresight error, and the user has the access to more computational hardware/software and

can accept longer simulation times, the modeling technique outlined in the authors' previous publication is recommended [19].

V. CONCLUSIONS

The benefits, of including discretization into the aperture integration, surface integration radome modeling technique have been demonstrated. Good agreement between far-field radiation patterns, boresight loss and boresight error predictions from CST and DrDaiSi has been shown. The notion of discretizing the aperture and radome extends the AiSi method's applicability to the analysis and design of airborne radomes which exist in the near-field of an enclosed antenna. Such near-field radome modeling would otherwise need to be performed with a full-wave method such as FIT, FDTD, MoM, or some other full-wave technique. In addition, the use of dyadic Green's functions as the field propagators was provided as a straightforward, matrix-math implementation.

Future research could include the hybridization of a full-wave solver to model the tip region; however, modeling the metal tip as a simple PEC blockage produced very good results for a fast and easily implementable high frequency approximation method. Additionally, the inclusion of a divergence factor to account for the growing outer radome surface facet area, as opposed to directly transporting fields from the inner to the outer radome surface via infinite flat planar transmission coefficients could provide improved transmission results. Fundamentally, all of these types of potential upgrades are still an approximation to the true electromagnetic interactions that occur. It is ultimately at the discretion of the radome engineer to decide when these approximations are valid, or when a full-wave technique must be used.

REFERENCES

- [1] M. A. Abdel Moneum, Z. Shen, J. L. Volakis, and O. Graham, "Hybrid PO-MoM analysis of large axi-symmetric radomes," *Antennas and Propagation, IEEE Transactions on*, vol. 49, no. 12, pp. 1657-1666, 2001.
- [2] A. Renuka and V. G. Borkar, "Computer-aided analysis for tangent Ogive airborne radome using physical optics method," *In Microwave Conference Proceedings, 2005, APMC 2005, Asia-Pacific Conference Proceedings*, vol. 5, pp. 4-pp., IEEE, 2005.
- [3] C. D. Finlay, S. Gregson, R. W. Lyon, and J. McCormick, "SPIKE a physical optics based code for the analysis of antenna radome interactions," *In Radar Systems, 2007 IET International Conference on*, pp. 1-5, IET, 2007.
- [4] H. F. Meng, W. Dou, and K. Yin, "Analysis of antenna-radome system at millimeter wave band," *In Millimeter Waves, 2008, GSMM 2008, Global Symposium on*, pp. 380-383, IEEE, 2008.
- [5] H. Meng and W. Dou, *Analysis and Design of Radome in Millimeter Wave Band*, Microwave and Millimeter Wave Technologies from Photonic Bandgap Devices to Antenna and Applications, Igor Minin (ed.), ISBN: 978-953-7619-66-4, InTech, DOI: 10.5772/9054, 2010.
- [6] H. F. Meng and W. Dou, "Rapid analysis of electrically large radome," *In Microwave and Millimeter Wave Technology (ICMMT), 2010 International Conference on*, pp. 99-101, IEEE, 2010.
- [7] H. F. Meng and W-B. Dou, "Fast analysis of electrically large radome in millimeter wave band with fast multipole acceleration," *Progress In Electromagnetics Research 120*, pp. 371-385, 2011.
- [8] T. Schuster and M. Sabielny, "REACH/PREACH—a physical optics based tool for simulation of radome effects on antenna patterns," *In Antennas and Propagation (EUCAP), 2012 6th European Conference on*, pp. 3225-3229, IEEE, 2012.
- [9] D. Paris, "Computer-aided radome analysis," *Antennas and Propagation, IEEE Transactions on*, vol. 18, no. 1, pp. 7-15, 1970.
- [10] D. C. Wu and R. Rudduck, "Plane wave spectrum-surface integration technique for radome analysis," *Antennas and Propagation, IEEE Transactions on*, vol. 22, no. 3, pp. 497-500, 1974.
- [11] J. A. Shifflett, "CADDRAD: a physical optics radar/radome analysis code for arbitrary 3D geometries," *Antennas and Propagation Magazine, IEEE*, vol. 39, no. 6, pp. 73-79, 1997.
- [12] L. Diaz and T. A. Milligan, *Antenna Engineering Using Physical Optics: Practical CAD Techniques and Software*, Artech House, Inc., 1996.
- [13] R. F. Harrington, *Time Harmonic Electromagnetic Fields*, McGraw-Hill Book Co., New York, 1961.
- [14] L. B. Felsen and N. Marcuvitz, *Radiation and Scattering of Waves*, Englewood Cliffs, NJ: Prentice-Hall, 1973.
- [15] C.A.Balanis, *Advanced Engineering Electromagnetics*, New York, NY: John Wiley & Sons, 1989.
- [16] C. A. Balanis, *Antenna Theory: Analysis and Design*, (3rd edition), New York, NY: John Wiley & Sons, 2005.
- [17] B. M. Kolundzija, "Electromagnetic modeling of composite metallic and dielectric structures," *Microwave Theory and Techniques, IEEE Transactions on*, vol. 47, no. 7, pp. 1021-1032, 1999.
- [18] D.J.Kozakoff, *Analysis of Radome-Enclosed Antennas*, Artech House Publishers, 2009.
- [19] B. L. Cannon and J. W. Jordan, "Integration of an equivalent aperture method into full-wave electromagnetic simulation of airborne radomes."
- [20] R. S. Elliott, *Antenna Theory and Design*, John

Wiley & Sons, 2003.



Jared Williams Jordan was born in Farmington, Maine on February 6, 1983. He received the B.S. degree in Electrical and Computer Engineering from University of Maine, Orono, ME, in 2005 and the M.S. degree in Electrical and Computer Engineering from University of Arizona, Tucson, AZ, in 2008. He has worked at Newpage Corporation as a Reliability Engineer (2005-2006) and at the University of Arizona as a Senior Research Engineer (2008-2010). He previously worked as a Senior Electrical Engineer at Raytheon Missile Systems, Tucson, AZ (2010-2014), and is currently an Associate Technical Staff at MIT Lincoln Laboratory, Lexington, MA in the Advanced

Technology Division: RF Technology (group 86). His current research interests include antenna and radome analysis and design, computational electromagnetics and material characterization.



Benjamin L. Cannon was born in McKeesport, PA in 1986. He received the B.S. degree in Electrical and Computer Engineering from Carnegie Mellon University, Pittsburgh, PA, in 2008 and the S.M. degree in Electrical Engineering from the Massachusetts Institute of Technology, Cambridge, MA in 2010. He previously worked as a Senior Electrical Engineer at Raytheon Missile Systems, Tucson, AZ (2010-2013), and is currently a Member of the Technical Staff at Nuvotronics, LLC, Durham, NC. He is interested in electromagnetic field and wave interactions with materials.